

1 **Seismic slip on an upper plate normal fault**

2 **during a large subduction megathrust rupture**

3 **Stephen P. Hicks\* and Andreas Rietbrock**

4 Liverpool Earth Observatory, University of Liverpool

5 Address: Jane Herdman Laboratories, 4 Brownlow Street, Liverpool, L69 3GP

6 **Email: [s.hicks@liverpool.ac.uk](mailto:s.hicks@liverpool.ac.uk)**

## 7 **Summary**

8 Quantification of stress accumulation and release during subduction zone seismic cycles  
9 requires an understanding of the distribution of fault slip during earthquakes. Reconstructions  
10 of slip are typically constrained to a single, known fault plane. Yet, slip has been shown to  
11 occur on multiple faults within the subducting plate<sup>1</sup> due to stress triggering<sup>2</sup>, resulting in  
12 phenomena such as earthquake doublets<sup>3</sup>. However, rapid stress triggering from the plate  
13 interface to faults in the overriding plate has not been documented. Here we analyse seismic  
14 data from the magnitude 7.1 Araucania earthquake that occurred in the Chilean subduction zone  
15 in 2011. We find that the earthquake, which was reported as a single event in global moment  
16 tensor solutions<sup>4,5</sup>, was instead composed of two ruptures on two separate faults. Within 12  
17 seconds, a thrust earthquake on the plate interface triggered a second large rupture on a normal  
18 fault 30 km away, in the overriding plate. This configuration of partitioned  
19 rupture is consistent with normal-faulting mechanisms in the ensuing aftershock sequence. We  
20 conclude that plate interface rupture can trigger almost instantaneous slip in the overriding plate  
21 of a subduction zone. This shallow upper plate rupture may be masked from teleseismic data,  
22 posing a challenge for real-time tsunami warning systems.

## 23 **Main body**

24 A recent succession of large ( $M_w > 8$ ) earthquakes in circum-Pacific subduction zones has  
25 focussed attention on the relationship between physical properties and stress distribution along  
26 the megathrust plate interface. Seismic ruptures along the megathrust can be viewed as smooth  
27 and spatially varying patches of slip on a single fault; in this case, the subducting plate  
28 interface<sup>6</sup>. The fault geometry used in early coseismic slip models is underpinned by centroid  
29 moment tensor (CMT) solutions often reported by earthquake monitoring agencies. Although  
30 more sophisticated slip inversions use curved faults based on regional subduction geometry<sup>7</sup>,  
31 slip is nearly always assigned to a single fault.

32 An alternative rupture configuration is slip occurring on separate faults due to static or dynamic  
33 triggering processes<sup>2</sup>, resulting in phenomena such as doublets<sup>3</sup>. A doublet is the occurrence of  
34 two nearby earthquakes with similar magnitude. The time delay between ruptures can range  
35 from months<sup>3</sup> to seconds<sup>1</sup>. Many documented cases of subduction zone doublets involve  
36 triggering between the subducting plate interface and deep-rooted faults in the downgoing  
37 plate<sup>3,8</sup>. Although the implications for tsunami hazard are significant, there are no reported cases  
38 of rapid triggering from the plate interface to the upper plate, where there are complex faulting  
39 networks<sup>9,10</sup>. To resolve triggered faulting in such cases, dense local seismic observations are  
40 needed.

41 A region with a suitably dense network of seismometers is the central Chile subduction zone  
42 following the  $M_w$  8.8 Maule earthquake in 2010. The ensuing aftershock sequence was captured  
43 in detail by the International Maule Aftershock Deployment<sup>11</sup>. Here, we focus on the largest  
44 interplate aftershock of the Maule sequence: the  $M_w$  7.1 Araucania earthquake that occurred on  
45 2 January 2011 at 20:20:18 UTC. Based on CMT solutions derived from teleseismic  
46 waveforms, the Araucania earthquake appears to be a ‘straightforward’ plate interface thrusting

47 event<sup>4,5</sup>. Its epicentre (Supplementary Note 1, Supplementary Table 1) lies in a region that acted  
48 as a barrier during the 1960  $M_w$  9.5 Valdivia<sup>12</sup> and 2010  $M_w$  8.8. Maule<sup>6,11</sup> earthquakes (Fig. 1).  
49 Moreover, the upper plate in this region is heavily faulted<sup>6,10</sup>. Therefore, the Araucania  
50 earthquake is an ideal candidate to examine possible interactions between the plate interface  
51 and upper plate faults.

52 We employed a multiple point-source inversion of regional seismic data<sup>13,14</sup>. Compared to  
53 conventional slip inversions along pre-defined fault planes<sup>6</sup> and single point-source CMT  
54 inversions<sup>5</sup>, we can retrieve centroid times of sub-events and permit multiple faulting styles on  
55 a grid of trial point-sources. A detailed understanding of 3-D crustal velocity structure<sup>15,16</sup>  
56 ensures robust waveform inversion. Synthetic tests (Supplementary Note 2) show that we can  
57 accurately resolve a range of extended source configurations involving offshore rupture using  
58 the available station distribution.

59 Using the observed data, we first investigated whether low-frequency waveforms (0.02–0.04  
60 Hz) in the near-field could represent the earthquake as a single point-source. The optimal  
61 regional CMT solution provides a good fit to the observed waveforms at most stations  
62 (Supplementary Figure 2). The centroid lies close to our relocated epicentre; its mechanism is  
63 consistent with the teleseismic GCMT and USGS solutions (Fig. 1), indicating thrusting along  
64 the plate interface. A high double-couple percentage (%DC) indicated by the global (98%) and  
65 our regional solutions (85%) suggests a simple faulting mechanism. When we increase the  
66 upper frequency limit to >0.06 Hz, waveform variance reduction (VR) sharply decreases and,  
67 at the upper limit of 0.08 Hz, we notice two clear arrivals in the observed waveforms (Fig. 1b  
68 & Supplementary Figure 3). Therefore, the next step is to consider whether a complex source  
69 can be resolved using higher frequency waveforms and a multiple point-source  
70 parameterisation.

71 A two-point-source model is a logical progression; an  $M_w \sim 7$  earthquake likely comprises no  
72 more than two to three patches of slip<sup>17</sup>. Compared with that of using the first source alone (VR  
73 = 0.57), introduction of the second source significantly increases the waveform fit (Fig. 2a) by  
74 30% (VR = 0.73), which is statistically significant to within the 99.5% confidence interval  
75 (Supplementary Note 3). Mechanisms at each trial point-source position are very consistent,  
76 with sharp correlation maxima (Fig. 2b). Based on our results, we can confidently identify the  
77 following sequence of events, which can be regarded as a closely-spaced doublet (CSD), both  
78 in time and space. Following nucleation, Event I ( $M_w$  6.8) ruptured the megathrust beneath the  
79 coast. No more than twelve seconds later, Event II ( $M_w$  6.7) ruptured to the southwest at a  
80 shallower depth and with an oblique normal faulting mechanism (Fig. 2).

81 Locations and mechanisms of aftershocks (Supplementary Note 4) that followed the Araucania  
82 earthquake support this CSD configuration. From our 44 relocated events, it is clear that there  
83 are two distinct groups of aftershocks (Fig. 3a). One group is located in the coastal region  
84 (hereafter, Group A); the other 30–40 km to the southwest (hereafter, Group B). Group B  
85 aftershocks have shallower depths, located within the marine forearc, up to 9 km above the  
86 plate interface (Fig. 3b). We obtained 19 robust CMT solutions from this aftershock sequence  
87 (Fig. 3), all of which have depths in agreement with their hypocentral location, based on a 3-D  
88 velocity model and ocean-bottom observations<sup>15</sup>. Normal faulting mechanisms dominate  
89 aftershock Group B. Group A aftershocks comprise mixed mechanisms, but interplate thrust  
90 faulting is most common.

91 A puzzling location discrepancy between Event II and aftershock Group B (Supplementary  
92 Figure 4) leads us to assess location bias in the multiple point-source inversion. So far, we have  
93 computed synthetic seismograms by calculating Green's functions in a 1-D velocity model.  
94 However, in the shallow regions of subduction zones, there are strong lateral velocity gradients  
95 (Figs. 3 & Supplementary Figure 5), particularly in S-wave velocity. Therefore, a more realistic

96 velocity model can improve waveform fits and make source inversions more stable. To account  
97 for lateral velocity variations, we simulated waveforms in a 3-D velocity model<sup>15,16</sup> using the  
98 spectral element code SPECFEM3D<sup>18</sup>. We used 3-D synthetics based on our two-point-source  
99 solution as input to a multiple point-source inversion using 1-D Green's functions. While the  
100 position of Event I remains stable, we find that the inversion shifts Event II 12 km to the south  
101 (from position 16 to 15; Supplementary Figure 6). Similarly, when we simulate the waveforms  
102 from Event II at the location of aftershock Group B (position 17), we find a similar southward  
103 shift, as implied from the real data inversion. Therefore, it is likely that Event II occurred ~12  
104 km northward with respect to the formal inversion result of Fig. 2b (Supplementary Table 5).  
105 This result demonstrates the importance of 3-D structural models to obtain accurate source  
106 parameters of offshore subduction earthquakes.

107 Based on our aftershock analyses and 3-D waveform simulations it is now clear that Event II  
108 ruptured on a normal fault near the base of the overriding crust (Figs. 3 & 4). Group B  
109 aftershocks are located close to the prominent Mocha-Villarrica fault zone (Fig. 3). This fault  
110 may be related to strong velocity contrasts in the marine forearc beneath Isla Mocha, where  
111 Group B aftershocks are located (Figs. 3 & 4). Crustal faulting in the region is pervasive and  
112 may extend through the entire crust<sup>10,19</sup>; it is plausible that the geometry of fault networks  
113 becomes more complex at the base of the forearc with possible conjugate faulting (Fig. 4). We  
114 speculate that these faults are compressional during the interseismic period, but a stress  
115 inversion following the Maule earthquake<sup>20</sup> may favour post-seismic extension. Based on  
116 approximate fault areas from scaling relations<sup>21</sup>, the two fault planes of Events I and II likely  
117 do not intersect. There are several possible mechanisms for the triggering of a rupture by a  
118 preceding earthquake. Dynamically triggered rupture of the normal fault is likely the dominant  
119 failure mechanism given that Event II's centroid time coincides with the passage of high-

120 amplitude S-wave arrivals from Event I (Supplementary Figure 7). However, we cannot  
121 completely rule out static stress transfer acting as a partial trigger.

122 To our knowledge, these results provide the first documented case of plate interface thrusting  
123 instantaneously activating a large rupture in the overriding plate through dynamic triggering.  
124 Past subduction zone doublets have been identified by high non-double components in their  
125 CMT solutions<sup>8</sup>. Conversely, in the case of the Araucania earthquake, the low-frequency single  
126 point-source solutions of both the global and regional CMT solutions did not yield a low %DC  
127 (Fig. 1). This discrepancy is also evidenced by our synthetic tests. It is possible that the short  
128 time delay and small distance between Events I and II masks rupture complexity in teleseismic  
129 CMT solutions. Therefore, CSDs may be completely hidden from global networks. CSDs may,  
130 however, be detected from a greater proportion of high frequency radiation in regional  
131 waveforms (Supplementary Note 5, Supplementary Figure 8), although this character may  
132 depend on several other source parameters, such as rupture duration. CMT solutions provided  
133 by global reporting agencies are accepted by the seismological community and form the basis  
134 of slip inversions and examinations of the stress field. CMTs are, therefore, a pillar of  
135 earthquake science, yet our results recommend their careful use in the case of slip on multiple  
136 fault planes.

137 The precedent set by this study also presents a new perspective for tsunami hazard assessment  
138 in subduction zones. Reverse faults as well as normal faults could theoretically be immediately  
139 triggered by megathrust slip, causing large seafloor displacement. A wide variety of upper plate  
140 faults are present in many subduction zones. For example, steeply-dipping normal faults have  
141 been imaged in the upper plate along the N. Chile and S. Peru margins<sup>9</sup>. Furthermore, a large  
142 upper-plate reverse faulting event preceded the 2014  $M_w$  8.2 Pisagua, N. Chile earthquake<sup>22</sup> and  
143 backthrust faults are widespread in the Sumatra subduction zone<sup>23</sup>. An  $M_w$  7.0 rupture in the  
144 upper plate could result in substantial vertical seafloor displacement of 1.2 m (Supplementary

145 Note 6). If this scenario were scaled up to a larger rupture ( $M_w \sim 7.5$ ), slip on the forearc fault  
146 could cause a localised tsunami on the continental shelf, although the upper limit of rupture size  
147 is controlled by the geometry and frictional properties of these faults (Fig. 3). A tsunami may  
148 be caused by static vertical displacement or through submarine landslides (Fig. 4), which have  
149 occurred locally in the past<sup>24</sup>. Yet without local strong-motion instruments, GPS networks, or  
150 close inspection of regional waveforms, near-field triggered ruptures will be difficult to detect.  
151 We speculate that the lack of evidence for Event II in single-source CMT solutions may result  
152 in part from the short timing between the two sources. Therefore, we recommend that the  
153 capability of teleseismic CMT inversions to resolve different doublet configurations is given a  
154 full assessment. Furthermore, there is a need to re-evaluate CMT solutions for large earthquakes  
155 using local and regional waveforms in subduction zones globally to examine whether CSDs  
156 involving the upper plate are ubiquitous.

157



- 159 1. Lay, T., Duputel, Z., Ye, L. & Kanamori, H. The December 7, 2012 Japan Trench intraplate  
160 doublet (Mw 7.2, 7.1) and interactions between near-trench intraplate thrust and normal  
161 faulting. *Phys. Earth. Planet. Inter.* **220**, 73–78 (2013).
- 162 2. Freed, A. M. Earthquake triggering by static, dynamic, and postseismic stress transfer.  
163 *Annu. Rev. Earth Planet. Sci.* **33**, 335–367 (2004).
- 164 3. Ammon, C. J., Kanamori, H. & Lay, T. A great earthquake doublet and seismic stress  
165 transfer cycle in the central Kuril islands. *Nature* **451**, 561–565 (2008).
- 166 4. United States Geological Survey National Earthquake Information Center. M7.2 -  
167 Araucania, Chile. (2011). at  
168 <[http://earthquake.usgs.gov/earthquakes/eventpage/usp000hsfq#scientific\\_tensor](http://earthquake.usgs.gov/earthquakes/eventpage/usp000hsfq#scientific_tensor)>
- 169 5. Ekström, G., Nettles, M. & Dziewoński, A. M. The global CMT project 2004–2010:  
170 Centroid-moment tensors for 13,017 earthquakes. *Phys. Earth. Planet. Inter.* **200-201**, 1–9  
171 (2012).
- 172 6. Moreno, M. *et al.* Toward understanding tectonic control on the Mw 8.8 2010 Maule Chile  
173 earthquake. *Earth Planet. Sci. Lett.* **321–322**, 152–165 (2012).
- 174 7. Hayes, G. P., Wald, D. J. & Johnson, R. L. Slab1. 0: A three- dimensional model of global  
175 subduction zone geometries. *J. Geophys. Res.* **117**, B1 (2012).
- 176 8. Lay, T. *et al.* The 2009 Samoa-Tonga great earthquake triggered doublet. *Nature* **466**, 964–  
177 968 (2010).
- 178 9. Audin, L., Lacan, P., Tavera, H. & Bondoux, F. Upper plate deformation and seismic  
179 barrier in front of Nazca subduction zone: The Chololo Fault System and active tectonics  
180 along the Coastal Cordillera, southern Peru. *Tectonophysics* **459**, 174–185 (2008).
- 181 10. Melnick, D., Bookhagen, B., Strecker, M. R. & Echtler, H. P. Segmentation of megathrust  
182 rupture zones from fore-arc deformation patterns over hundreds to millions of years,  
183 Arauco peninsula, Chile. *J. Geophys. Res. Solid Earth* **114**, B01407 (2009).
- 184 11. Rietbrock, A. *et al.* Aftershock seismicity of the 2010 Maule Mw= 8.8, Chile, earthquake:  
185 Correlation between co-seismic slip models and aftershock distribution? *Geophys. Res.*  
186 *Lett.* **39**, L08310 (2012).
- 187 12. Moreno, M. S., Bolte, J., Klotz, J. & Melnick, D. Impact of megathrust geometry on  
188 inversion of coseismic slip from geodetic data: Application to the 1960 Chile earthquake.  
189 *Geophys. Res. Lett.* **36**, L16310 (2009).
- 190 13. Sokos, E. & Zahradnik, J. A Matlab GUI for use with ISOLA Fortran codes. *Users' guide*  
191 (2006).
- 192 14. Zahradnik, J., Serpetsidaki, A., Sokos, E. & Tselentis, G.-A. Iterative Deconvolution of  
193 Regional Waveforms and a Double-Event Interpretation of the 2003 Lefkada Earthquake,  
194 Greece. *B. Seismol. Soc. Am.* **95**, 159–172 (2005).
- 195 15. Hicks, S. P., Rietbrock, A., Ryder, I. M. A., Lee, C.-S. & Miller, M. Anatomy of a  
196 megathrust: The 2010 M8.8 Maule, Chile earthquake rupture zone imaged using seismic  
197 tomography. *Earth Planet. Sci. Lett.* **405**, 142–155 (2014).
- 198 16. Haberland, C., Rietbrock, A., Lange, D., Bataille, K. & Dahm, T. Structure of the  
199 seismogenic zone of the southcentral Chilean margin revealed by local earthquake

- 200 traveltime tomography. *J. Geophys. Res.* **114**, B01317 (2009).
- 201 17. Zahradnik, J. & Sokos, E. The Mw 7.1 Van, Eastern Turkey, earthquake 2011: two-point  
202 source modelling by iterative deconvolution and non-negative least squares. *Geophys. J.*  
203 *Int.* **196**, 522–538 (2014).
- 204 18. Komatitsch, D., Erlebacher, G., Göddeke, D. & Michéa, D. High-order finite-element  
205 seismic wave propagation modeling with MPI on a large GPU cluster. *J. Comput. Phys.*  
206 **229**, 7692–7714 (2010).
- 207 19. Hicks, S. P., Nippres, S. E. & Rietbrock, A. Sub-slab mantle anisotropy beneath south-  
208 central Chile. *Earth Planet. Sci. Lett.* **357**, 203–213 (2012).
- 209 20. Hardebeck, J. L. Coseismic and postseismic stress rotations due to great subduction zone  
210 earthquakes. *Geophys. Res. Lett.* **39**, L21313 (2012).
- 211 21. Blaser, L., Krüger, F., Ohrnberger, M. & Scherbaum, F. Scaling Relations of Earthquake  
212 Source Parameter Estimates with Special Focus on Subduction Environment. *B. Seismol.*  
213 *Soc. Am.* **100**, 2914–2926 (2010).
- 214 22. González, G. *et al.* Upper plate reverse fault reactivation and the unclamping of the  
215 megathrust during the 2014 northern Chile earthquake sequence. *Geology* G36703.1  
216 (2015).
- 217 23. Singh, S. C. *et al.* Evidence of active backthrusting at the NE Margin of Mentawai Islands,  
218 SW Sumatra. *Geophys. J. Int.* **180**, 703–714 (2010).
- 219 24. Geersen, J., Völker, D., Behrmann, J. H., Reichert, C. & Krastel, S. Pleistocene giant slope  
220 failures offshore Arauco Peninsula, Southern Chile. *J. Geol. Soc. London* **168**, 1237–1248  
221 (2011).
- 222 25. Quintero, R., Zahradnik, J. & Sokos, E. Near-regional CMT and multiple-point source  
223 solution of the September 5, 2012, Nicoya, Costa Rica Mw 7.6 (GCMT) earthquake. *J. S.*  
224 *Am. Earth Sci.* **55**, 155–165 (2014).
- 225 26. Sokos, E. & Zahradnik, J. Evaluating Centroid- Moment- Tensor Uncertainty in the New  
226 Version of ISOLA Software. *Seismol. Res. Lett.* **84**, 656–665 (2013).
- 227 27. Casarotti, E. *et al.* in *Proceedings of the 16th International Meshing Roundtable* 579–597  
228 (Springer Berlin Heidelberg, 2008).
- 229 28. Frohlich, C. Triangle diagrams: ternary graphs to display similarity and diversity of  
230 earthquake focal mechanisms. *Phys. Earth. Planet. Inter.* **75**, 193–198 (1992).
- 231 29. Hayes, G. P. *et al.* Seismotectonic framework of the 2010 February 27 Mw 8.8 Maule,  
232 Chile earthquake sequence. *Geophys. J. Int.* **195**, 1034–1051 (2013).
- 233 30. Melnick, D. & Echtler, H. P. in *The Andes* 565–568 (Springer Berlin Heidelberg, 2006).  
234 doi:10.1007/978-3-540-48684-8\_30
- 235

## 236 **Supplementary information**

237 Supplementary information is linked to the online version of the paper at  
238 [www.nature.com/nature](http://www.nature.com/nature).

## 239 **Acknowledgments**

240 We are grateful to all field crews from partner organisations who participated in the deployment  
241 and servicing of seismic instruments used in this study. We thank Jiří Zahradník and Efthimios  
242 Sokos for their assistance in setting up the ISOLA code. S.P.H. is funded by a NERC  
243 studentship NE/J50015X/1.

## 244 **Author contributions**

245 S.P.H. carried out the single and multiple point-source inversions, as well as the moment tensor  
246 inversion and aftershock relocations. S.P.H. wrote the manuscript, interpreted the results, and  
247 generated all figures. A.R. carried out the 3-D full waveform simulations, wrote the manuscript,  
248 and interpreted the results.

## 249 **Author information**

250 Reprints and permissions information is available at [www.nature.com/reprints](http://www.nature.com/reprints).

251 The authors declare no competing financial interests.

252 Correspondence and requests for materials should be addressed to S.P.H.  
253 ([s.hicks@liverpool.ac.uk](mailto:s.hicks@liverpool.ac.uk)) or A.R. ([a.rietbrock@liverpool.ac.uk](mailto:a.rietbrock@liverpool.ac.uk)).

254



Fig. 1: Location and single source solution. a) Location map. Stations used for CMT inversion are labelled with station codes. Other stations are for hypocentre relocation only (Supplementary Note 1). Shading indicates rupture areas of great earthquakes in 1960<sup>12</sup> and 2010<sup>6</sup>. Inset: Regional tectonic setting. b) Double-couple percentage (%DC) and variance reduction (VR) of the single point-source versus frequency. A transition occurs at 0.057 Hz, where VR suddenly decreases because the waveforms cannot be explained by a single source alone. This change is illustrated by representative waveforms at low and high frequencies (see Supplementary Figure 2 & Supplementary Figure 3 for details).

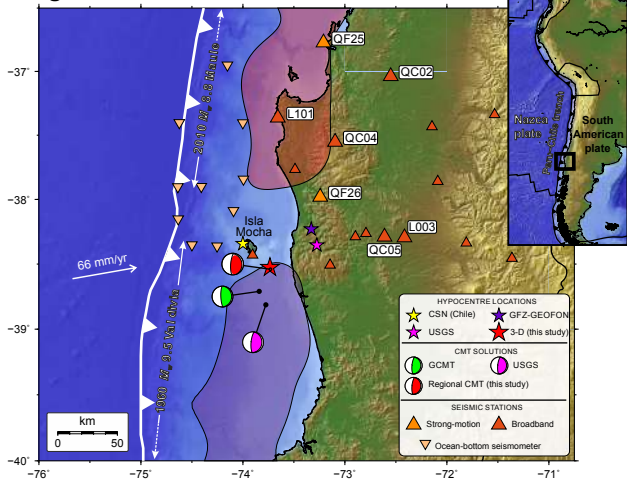
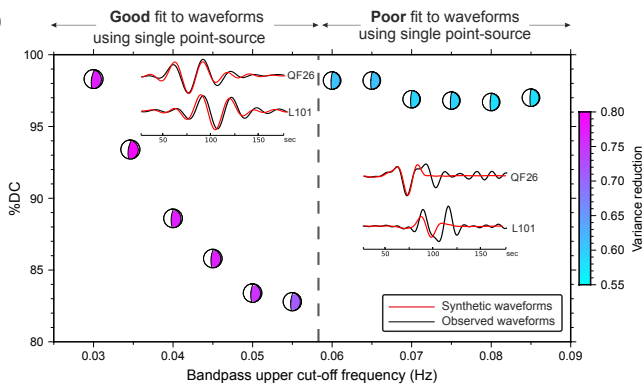
256

Fig. 2: Two-point-source solution. a) Observed (black) and synthetic (red) waveforms for the optimum high-frequency (0.02–0.08 Hz) solution. Station names are labelled. Numbers alongside each waveform component denote VR. Blue and green shading denotes the contribution from each event. b) Waveform correlation for each event as a function of trial point-source position (numbered). The optimum time shift of Event I and II is shown. Black beach balls are solutions that lie within 90% of the optimum solution's (red beach ball) VR. The red star denotes the earthquake's epicentre. c) Resulting moment-rate function obtained using the NNLS method.

257

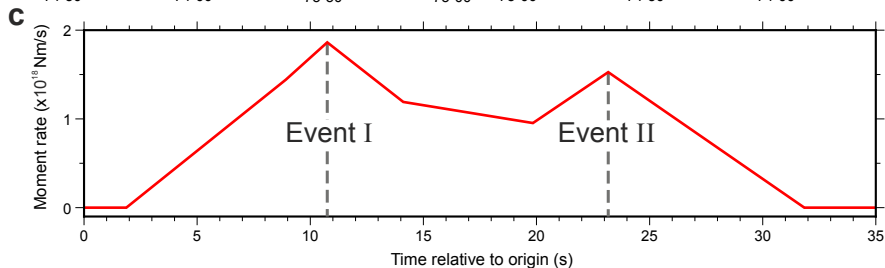
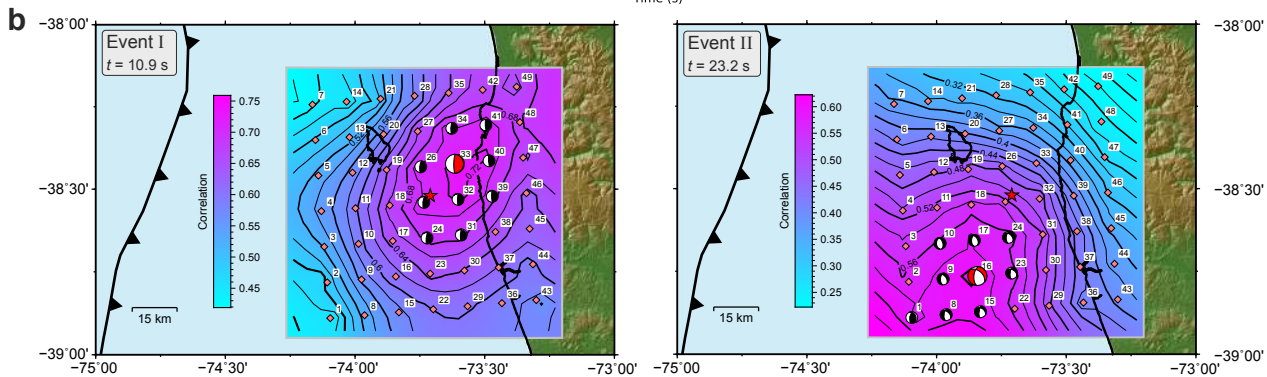
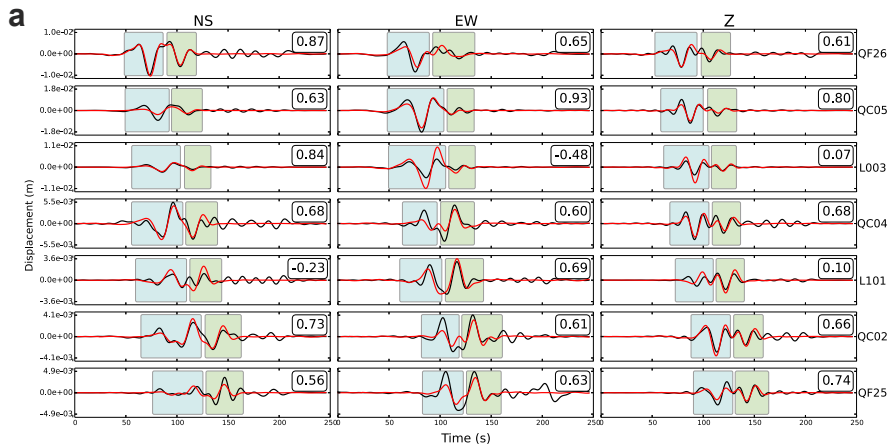
Fig. 3: Aftershock analysis. (a) Map and (b) cross-section showing locations and focal mechanisms of aftershocks (Groups A and B) and mainshock events (labelled EV-I and EV-II). Faulting style is classified on principal stress orientations<sup>28</sup> and minimum rotation angle with respect to plate interface thrust faulting<sup>29</sup>, accounting for plate interface geometry (black line)<sup>15,16</sup>. We plot the revised location of Event II, based on 3-D waveform modelling. Mapped faults are shown<sup>10,30</sup>; MVFZ = Mocha-Villarrica fault zone. The cross-section background is from P-wave velocity tomography models<sup>15,16</sup>. The star denotes the hypocentre of the Araucania earthquake; the triangle shows the coastline.

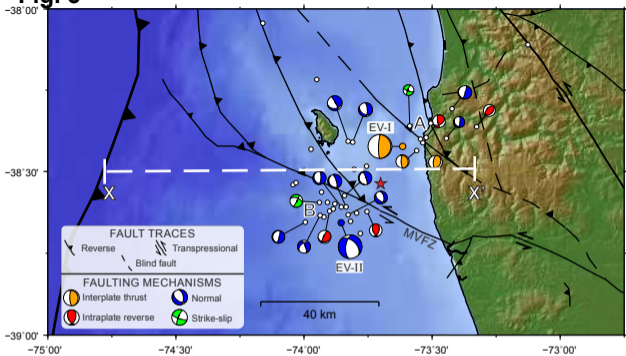
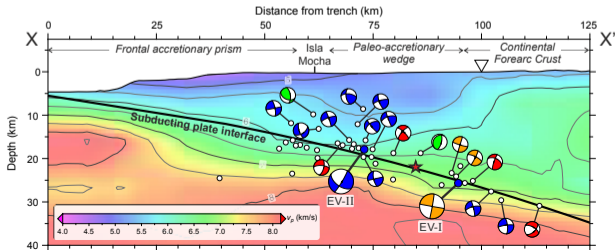
Fig. 4: Schematic interpretation of the Araucania earthquake rupture. Plate interface thrusting (Event I) triggered a rupture along an extensional fault in the overriding plate (Event II). It is likely that two great earthquakes in 1960 and 2010 brought both faults closer to failure. As shown by ancient submarine landslide deposits in the area, a larger-scale rupture in the overriding plate has the potential to act as a tsunamigenic earthquake. Beach balls represent the focal mechanisms of both events from Fig. 3. The inset shows the interpreted structure of conjugate normal faulting with the background colour representing  $v_p/v_s$  ratio<sup>15</sup>.

**a** Fig. 1**b**



**Fig. 2**



**a Fig. 3****b**

**Fig 4.**

Vertical exaggeration: 2.5x

Horizontal scale:

40 km

Slope failure deposits  
(Geersen et al., 2011)1960 M9.5 Valdivia earthquake  
rupture area2010 M8.8 Maule earthquake  
rupture area

Depth (km)

0  
10  
20  
30  
40

Coastline

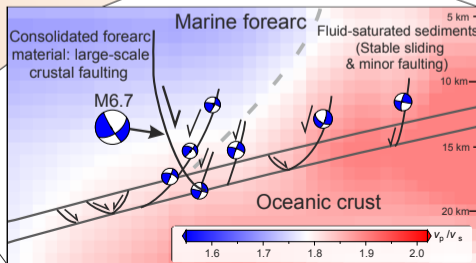
Isla Mocha

Marine forearc

Trench

Oceanic  
Nazca  
crustContinental  
forearc  
crust(1) Rupture  
nucleation(3) Extensional  
rupture in  
overriding plate(2) Plate interface  
thrust rupture

Plate interface Seismogenic zone



## 261 **Methods**

### 262 **Data selection and processing**

263 For the waveform inversion of the Araucania earthquake, we used broadband and strong-motion  
264 stations that were located onshore within an epicentral distance of 200 km from the Araucania  
265 earthquake. We only used waveforms from stations that have a high signal-to-noise ratio ( $> 10$ )  
266 in the frequency range 0.01–0.10 Hz (Supplementary Figure 9). Due to the close proximity of  
267 some stations to the earthquake, we excluded waveform records that were either clipped, had  
268 long period disturbances, or instrument tilt effects. These quality-control checks resulted in a  
269 set of seven stations (including two strong-motion stations) located north and east of the  
270 Araucania earthquake (Fig. 1a).

### 271 **Source inversion algorithm**

272 Iterative deconvolution (ID)<sup>14</sup> is used for the multiple point-source inversion of deviatoric  
273 moment tensors. ID works by inverting for the optimum focal mechanism and timing of sources  
274 for a prescribed set of points to minimise the L2 misfit between observed and synthetic  
275 waveforms. A grid search is then performed to select the source position that produces the  
276 highest correlation between observed and synthetic waveforms. The first inversion explains the  
277 full waveforms using a single source, the synthetics of which are then subtracted from the  
278 observed waveforms. The remaining waveforms are then used to invert for subsequent sub-  
279 events<sup>14</sup>. After the retrieval of each sub-event, VR is calculated and manually assessed to ensure  
280 that additional sub-events are required by the data and the waveforms are not just fitting  
281 correlated noise. For moment tensor inversion, we use the software package, ISOLA<sup>13</sup>, which  
282 can be accessed at <http://seismo.geology.upatras.gr/isola/>. In the inversion, the moment-rate of  
283 the source is prescribed; it is found by manually searching for the source length that produces  
284 the maximum VR. If the moment-rate of the source is shorter than the minimum inverted period,

285 then the source can be represented by a delta function. To negate artifacts produced by the ID  
286 method, we also test the stability of our multiple point-source solution using a non-negative  
287 least squares (hereafter, NNLS) inversion method<sup>17</sup>. In the NNLS approach, the double-couple  
288 focal mechanism at each source is prescribed. At each trial point-source position, the moment  
289 rate is represented by a set of shifted triangles. The weight of each triangle is then inverted for  
290 using NNLS. In this paper, we use one-second triangle shifts. The moment of each source can  
291 be constrained, which stabilises the inversion, although the exact value of total moment does  
292 not dramatically influence source timings or positions<sup>25</sup>.

293 The inversion is performed on bandpass-filtered displacement waveforms. The effect of  
294 different 1-D velocity models was tested; the final solutions were calculated using a velocity  
295 model appropriate for the coastline of south-central Chile (Supplementary Figure 10). We  
296 analysed the effect of data errors and imperfect Green's functions by systematically removing  
297 pieces of data from the inversion (jackknifing). Where subsurface structure is complex, removal  
298 of certain stations may have a large effect on the final solution<sup>26</sup>. Based on the analysis of signal  
299 to noise ratio (Supplementary Figure 9), we used a lowermost frequency limit of 0.02 Hz  
300 throughout this paper. The upper frequency limit was dependent on the source parameterisation  
301 used (single or multiple source).

### 302 **Single point-source inversion strategy**

303 Guided by preliminary inversions and the anticipated fault size<sup>21</sup>, we used a trial point-source  
304 grid with a spacing of 12 km in the down-dip and along-strike directions (Fig. 2b). At this stage,  
305 we wanted to resolve the simplest possible source, so the maximum frequency was kept well  
306 below the corner frequency (approximately 0.1 Hz for an  $M_w \sim 7$  earthquake). Therefore, we  
307 chose an upper frequency limit of 0.04 Hz and assumed a delta moment-rate function. We tested  
308 the robustness of the solution by jackknifing stations and their individual components. The

309 source position changes slightly when varying the dataset, but by no more than 17 km  
310 (Supplementary Figure 2); the largest shifts occur if the closest stations are removed from the  
311 inversion. The zone of maximum correlation is not particularly sharp, corresponding to the  
312 possible source locations from the jackknifing analysis (Supplementary Figure 2). These tests  
313 show that the source location is reasonably stable and its mechanism is consistent throughout.

314 We also find that as the upper frequency bandpass cut-off increases, %DC gradually decreases.  
315 This trend continues until around 0.057 Hz, above which, the full waveforms can only be  
316 explained using Events I and II, and %DC becomes very high (Fig. 1b).

### 317 **Multiple point-source inversion strategy**

318 We first carried out a multiple point-source inversion using ID, in which the deviatoric moment  
319 tensor mechanisms of both sources were allowed to vary. The grid of point-sources was kept  
320 the same as for the single point-source inversion. For the source-time function, we found that  
321 with increasing length of the triangle, the total moment gradually increases, while VR and %DC  
322 of each source reaches a maximum at 18 s (Supplementary Figure 11). We therefore fixed the  
323 triangle length of each source to 18 s for the ID multiple point-source inversion, although the  
324 point-source mechanisms remain consistent for different triangle lengths, suggesting a stable  
325 solution.

326 We used the NNLS method to test the robustness of the solution obtained by ID. To search for  
327 the best-fitting source configurations, we performed two inversions: one in which total moment  
328 was constrained by the ID solution; the other in which moment was allowed to vary. We tested  
329 a number of source positions and faulting styles for Events I and II using the NNLS method,  
330 but we found that the highest VR came from the two-point-source configuration found using  
331 the ID method. Using the mechanisms given by the ID solution, we then performed a grid-  
332 search over all possible combinations of the two-point-source locations using the NNLS

333 method. As expected, the moment-constrained inversion is most similar to the ID solution  
334 (Supplementary Figure 12). Nevertheless, both inversions produce results consistent with the  
335 ID solution. Importantly, the resulting source-time function obtained by NNLS shows that both  
336 events have a similar time function to the 18 s triangle source used in ID (Fig. 2c). In summary,  
337 we find no bias in the results caused by the inversion method.

338 As a further test of solution stability, we perform jackknifing tests by removing one station at  
339 a time from the inversion. The results of these tests are shown in Supplementary Table 6 and  
340 demonstrate remarkably consistent centroid positions and focal mechanisms for Events I and  
341 II. The jackknifing test therefore indicates that the optimum multiple point-source solution is  
342 not dependent on one single waveform. Furthermore, a three-point-source approximation did  
343 not meaningfully improve the waveform fit ( $VR = 0.76$ ; 3% increase in VR compared with  
344 two-point-sources).

345 Since the ID method inverts for the first point-source before subsequently calculating the  
346 second source, we carried out a test to determine whether Event II is dependent on the chosen  
347 location and mechanism of Event I. Normally, we accept the source position that produces the  
348 highest waveform correlation. However, for this test, we fixed the position of Event I and chose  
349 the corresponding best-fitting mechanism. We carried out this test at all trial point-sources  
350 adjacent to Position 33 (the optimum position of Event I). The results of this test are shown in  
351 Supplementary Table 7. For all but one position of Event I, the position, timing, and mechanism  
352 of Event II remain consistent with the optimum solution. When Event I is fixed to Position 25,  
353 the MT solution of Event II appears less stable. However, Position 25 is directly adjacent to  
354 Position 16 (the optimum location of Event II from ID; Fig. 2b), so this discrepancy is expected  
355 because the inversion tries to explain both events at this position with a single source. In  
356 summary, we find that the Event II solution is stable with respect to the exact position and  
357 mechanism of Event I.

### 358 **Mesh design for the 3-D waveform simulation**

359 For the wave propagation simulations, we constructed a hexahedral unstructured mesh using  
360 the GEOCUBIT software package<sup>27</sup>. The lateral resolution at the surface is 5 km, coarsening at  
361 a refinement layer (45 km depth, which is an average Moho depth for the region<sup>15,16</sup>). The mesh  
362 honours surface relief and bathymetry to ensure that topographic effects on waveform  
363 propagation are accurately simulated. Our mesh does not contain dipping geological  
364 discontinuities in the subsurface, such as the oceanic Moho, due to the lack of constraints on its  
365 geometry. This mesh has been designed for simulations that are accurate up to  $\sim 0.3$  Hz, well  
366 above the maximum frequency of our waveform inversions, ensuring numerically stable  
367 simulations. The Mesh used is shown in Supplementary Figure 13.